1

Advanced Topics in Sediment Transport Modelling: Non-alluvial Beds and Hyperconcentrated Flows

B. Dewals, F. Rulot, S. Erpicum, P. Archambeau and M. Pirotton
Hydrology, Applied Hydrodynamics and Hydraulic Constructions, University of Liège, Chemin des Chevreuils 1, B52/3+1 - B-4000 Liège, Belgium

1. Introduction

Civil and environmental engineers frequently face sediment transport issues such as local scouring, sedimentation in reservoirs, erosion after floods or dam breaching flows as well as long term aggradation or degradation of riverbed (Dewals et al. 2010b; van Rijn 2007; White 2001). Such sediment related problems are of huge importance in most projects of river engineering, calling for structures to be designed considering sediment transport issues from the very early stages of project development. Sustainable operation rules also need to be developed, both in short and long term perspectives. As a result of the complexity of the governing physical processes and the significant uncertainties affecting input data, modeling tools with a genuine predictive capacity, such as comprehensively validated numerical models, constitute key elements to provide quantitative decision-support in project design and developments.

Sediment transport has been studied from a physical point of view for almost two hundred years but is not yet fully understood (Frey and Church 2009). In particular, while the Navier-Stokes and continuity equations represent a generally accepted mathematical description of fluid flow, there is no comparable model for the complete interaction of flow, sediment transport and bed evolution (Spasojevic and Holly 2008). Therefore, sediment transport remains a challenging topic of research today, since a unified description of processes is still to be achieved. In this quest, both new experimental approaches and more advanced numerical models have a part to play; the former providing new insight into fundamental processes while the later enabling to upscale the results for real-life applications.

In this chapter, we first present an original two-phase flow model for the water-sediment mixture, acting as a unified basis for all our subsequent developments. Next, we focus on two topics in which we have made original contributions, namely sediment routing on alluvial and non-alluvial beds and modelling of transient hyperconcentrated flows. In both cases, we use our original two-phase flow modelling framework to derive specific governing equations, for which we detail an appropriate finite volume numerical scheme and demonstrate their validity through a number of test cases.

2. Two-phase flow model for water-sediment mixtures

In this section, we subsequently review existing mathematical models for sediment-laden flows, including two-phase flow theories, present our own two-phase flow morphodynamic model and eventually detail its mathematical properties together with its numerical discretization.

2.1 Existing mathematical models

Cao and Carling (2002a) have provided a comprehensive discussion of existing approaches for mathematical modelling of sediment-laden flows. They have emphasized a number of shortcomings, particularly with respect to the turbulence closure models and the bottom boundary conditions. The former fail to reproduce the intricate interactions between the sediments and the flow turbulence; while the formulation of the later is affected by a high level of uncertainty as detailed in their companion paper (Cao and Carling 2002b). Existing numerical models also generally rely on simplifications in the water-sediment mixture and global sediment continuity equations: respectively, ignored time derivative of the bottom elevation and neglected sediment storage in the water column. These assumptions become questionable when significantly transient processes take place.

In contrast with other fields of hydraulic engineering such as aerated flows (Kerger et al. 2010b), the governing equations underlying most existing models for sediment-laden flows stem from single-phase flow theory. They involve continuity and momentum equations for clear water, combined with a continuity equation for sediments (Spasojevic and Holly 2008). They are therefore only valid for low sediment concentrations (<0.1 in volume) (Greimann and Holly 2001). Although water-sediment mixtures constitute obviously two-phase media, only very few attempts to account explicitly for this multiphase nature have been reported in sediment transport models and hardly none in morphodynamic models.

Two-phase flow models for sediment transport

In a two-phase formulation, Cao et al. (1995) derived suspended sediment concentration profiles valid for both low and high concentrations. Importance was stressed on the influence of the closure relations for turbulent viscosity and diffusivity. Similarly, Greimann et al. (1999) explained the increased diffusive flux of large particles and measurable velocity lag of particles (drift velocity), two observed phenomena but theoretically unexplained so far. A generalized mathematical model for the liquid-solid mixture was derived by Wu and Wang (2000) based on the two-fluid model, but validation and application were not reported. Greimann and Holly (2001) accounted for both particle-particle interactions and particle inertia in the expression of equilibrium concentration profiles for suspended sediments. Still, empiricism was necessary to formulate the turbulence quantities and they highlighted the need for further experimental and analytical work to develop improved models for the fluid eddy viscosity, relative magnitude of the particle turbulence intensity and boundary conditions applicable to loose beds. Criteria were given to determine if particle-particle interactions and particle inertia are significant. Recently, Bombardelli and Jha (2009) showed that both a standard sediment-transport model and a two-fluid-model predict accurately the velocity field, whereas only the later provides satisfactory predictions for the concentration profiles and the turbulence statistics. Extending to two-phase flows the well-known results of single-phase flows in open channels, they also found that the Reynolds stress model does not improve the predictions beyond the accuracy of the standard $k-\varepsilon$ model, at least for dilute mixtures. Values of the Schmidt number that fit the

datasets indicate that the eddy viscosity is smaller than the diffusivity of sediment (Bombardelli and Jha 2009), which is in agreement with part of the literature but not all (Cao and Carling 2002a; Cao and Carling 2002b).

Two-phase morphodynamic models

Two-phase formulations for complete morphodynamic models are hardly available in literature. Recently, Greco et al. (2008) presented a 1D single layer two-phase morphodynamic model, which they successfully applied for dam break flow over an erodible topography.
A more rigorous theoretical derivation of a general two-phase flow model for flows in hydraulic environmental engineering has also been presented by Kerger, Dewals et al. (2011), but validation and applications have not yet been reported.

Double-averaged models

The double-averaging concept was recently introduced in hydraulic engineering by Nikora et al. (2007) and current research suggests that it may become a standard tool for fluvial applications. By means of explicit consideration of roughness mobility and form-induced stresses stemming from a rigorous derivation, the approach provides an enhanced treatment of the bed shear stress formulation, which will prove valuable for morphodynamic modelling. Nonetheless, using the double-averaged hydrodynamic equations for developing numerical models is still in its infancy and closures for subgrid scale effects remain to be developed (Walters and Plew 2008).

2.2 Derivation of an original two-phase flow model

In the following paragraphs, we detail the derivation of a two-phase mathematical model for flow, sediment transport and morphodynamics. The finite volume numerical technique developed to solve the set of governing equations is also detailed, together with a comparative discussion of synchronous vs. sequential resolution of the flow, sediment transport and morphodynamic models.

Conservation laws

Following an Eulerian description of the flow, we formulate conservation laws for the flow in a Cartesian system of coordinates (x, y, z), as sketched in Fig. 1.

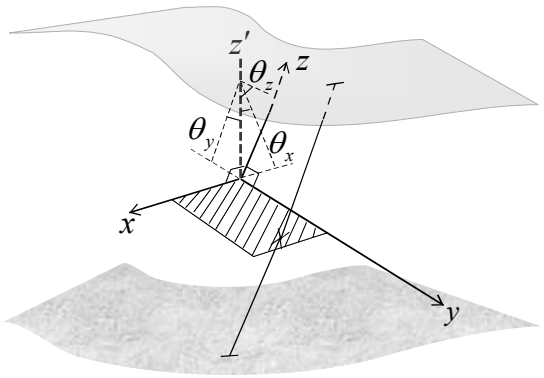

Fig. 1. Axis of reference.

The x and y axes are chosen in such a way that the plane they define corresponds to the main flow direction. Axis z is simply set normal to this plane. The axes x, y and z are inclined of angles θ_x, θ_y and θ_z with respect to the vertical direction (axis z'). In the particular case where the x-y plane is horizontal the angles become: $\theta_x = \theta_y = 0$ and $\theta_z = \pi / 2$.
The Reynolds-averaged mass and momentum conservation equations for the water-sediment mixture read:

$$\frac{\partial \rho}{\partial t} + \frac{\partial (\rho u)}{\partial x} + \frac{\partial (\rho v)}{\partial y} + \frac{\partial (\rho w)}{\partial z} = 0 \tag{1}$$

$$\begin{aligned}
&\frac{\partial (\rho u)}{\partial t} + \frac{\partial \left(\rho u^2\right)}{\partial x} + \frac{\partial (\rho uv)}{\partial y} + \frac{\partial (\rho uw)}{\partial z} = -\frac{\partial p}{\partial x} + \frac{\partial \sigma_x}{\partial x} + \frac{\partial \tau_{xy}}{\partial y} + \frac{\partial \tau_{xz}}{\partial z} + \rho g \sin\theta_x \\
&\frac{\partial (\rho v)}{\partial t} + \frac{\partial (\rho uv)}{\partial x} + \frac{\partial \left(\rho v^2\right)}{\partial y} + \frac{\partial (\rho vw)}{\partial z} = -\frac{\partial p}{\partial y} + \frac{\partial \tau_{yx}}{\partial x} + \frac{\partial \sigma_y}{\partial y} + \frac{\partial \tau_{yz}}{\partial z} + \rho g \sin\theta_y \\
&\frac{\partial (\rho w)}{\partial t} + \frac{\partial (\rho uw)}{\partial x} + \frac{\partial (\rho vw)}{\partial y} + \frac{\partial \left(\rho w^2\right)}{\partial z} = -\frac{\partial p}{\partial z} + \frac{\partial \tau_{zx}}{\partial x} + \frac{\partial \tau_{zy}}{\partial y} + \frac{\partial \sigma_z}{\partial z} - \rho g \sin\theta_z
\end{aligned} \tag{2}$$

with ρ = mixture density; u, v and w = velocity components along x, y and z; g = gravity acceleration; p = pressure; σ_i = Reynolds normal stresses ($i = x, y, z$); τ_{ij} = Reynolds shear stresses ($i, j = x, y, z$). Viscous stresses in the momentum equations have been neglected compared to Reynolds stresses since the later greatly excess the former in practical applications.
Conservation of a dispersed phase in the fluid, namely suspended sediments, is expressed by the following advection-diffusion equation:

$$\frac{\partial (\rho\phi)}{\partial t} + \frac{\partial (\rho u\phi)}{\partial x} + \frac{\partial (\rho v\phi)}{\partial y} + \frac{\partial}{\partial z}\left[\rho\left(w - w_s\right)\phi\right] = -\left(\frac{\partial \tilde{q}^{\mathrm{d}}_{\phi,x}}{\partial x} + \frac{\partial \tilde{q}^{\mathrm{d}}_{\phi,y}}{\partial y} + \frac{\partial \tilde{q}^{\mathrm{d}}_{\phi,z}}{\partial z}\right) + \tilde{S}_{\phi}\,., \tag{3}$$

in which ϕ = mass concentration and w_s = settling velocity of sediments. Notations $\tilde{q}^{\mathrm{d}}_{\phi,x}$, $\tilde{q}^{\mathrm{d}}_{\phi,y}$ and $\tilde{q}^{\mathrm{d}}_{\phi,z}$ refer to the mass fluxes induced by turbulence, which are usually evaluated as follows:

$$\tilde{q}^{\mathrm{d}}_{\phi,x} = \frac{\nu_{\mathrm{T}}}{\sigma_{\mathrm{T}}}\frac{\partial \phi}{\partial x}, \quad \tilde{q}^{\mathrm{d}}_{\phi,y} = \frac{\nu_{\mathrm{T}}}{\sigma_{\mathrm{T}}}\frac{\partial \phi}{\partial y} \quad \text{and} \quad \tilde{q}^{\mathrm{d}}_{\phi,z} = \frac{\nu_{\mathrm{T}}}{\sigma_{\mathrm{T}}}\frac{\partial \phi}{\partial z}, \tag{4}$$

with σ_{T} the Schmidt number taking typical values in-between 0.8 and 1.2 (e.g. Hervouet 2003). The notation $\tilde{S}_{\phi}$ designates the production rate within the flow layer, which is usually zero for non-reactive flows.

Depth-averaging concept

Most flows of interest in civil and environmental engineering are characterized by significantly larger length scales in a reference plane (often almost horizontal) compared to the characteristic depth of the flow. This motivates the use of depth-averaged models, which require far less intricate numerical resolution procedures than needed for general three-

dimensional free surface flows. In addition, besides reducing the complexity of the model, such a depth-averaged description of the flow better fits with available data and outputs of interest for most applications in civil and environmental engineering.

Bottom and free surface boundary conditions

Deriving a depth-averaged model from equations (1)-(3) requires boundary conditions to be prescribed at the bottom ($z = z_b$) and at the free surface ($z = z_s$). These include kinematic boundary conditions expressed as follows:

$$\frac{\partial z_b}{\partial t} + u\frac{\partial z_b}{\partial x} + v\frac{\partial z_b}{\partial y} - w = r_b \,, \tag{5}$$

$$\frac{\partial z_s}{\partial t} + u\frac{\partial z_s}{\partial x} + v\frac{\partial z_s}{\partial y} - w = 0 \,, \tag{6}$$

with r_b (m/s) the exchange flux with the bed; z_b and z_s the bed and surface elevations respectively. Note that $\partial z_b/\partial t$ has not been set to zero in (5) since we deal here with flows over erodible beds.

Since wind effects are not considered here, dynamic boundary conditions at the free surface simply state that pressure remains equal to the atmospheric pressure and that both normal and shear stresses are zero. Dynamic boundary conditions at the bottom link the components of the stress tensor with the bottom shear stress $\boldsymbol{\tau}_b$ per unit horizontal surface:

$$\begin{aligned}
\tau_{bx}\,\Delta\Sigma &= \sigma_x\frac{\partial z_b}{\partial x} + \tau_{xy}\frac{\partial z_b}{\partial y} - \tau_{xz} \\
\tau_{by}\,\Delta\Sigma &= \tau_{xy}\frac{\partial z_b}{\partial x} + \sigma_y\frac{\partial z_b}{\partial y} - \tau_{yz} \\
\tau_{bz}\,\Delta\Sigma &= \tau_{xz}\frac{\partial z_b}{\partial x} + \tau_{yz}\frac{\partial z_b}{\partial y} - \sigma_z \,,
\end{aligned} \tag{7}$$

where notation $\Delta\Sigma$ stands for $\sqrt{1+\left(\partial z_b/\partial x\right)^2+\left(\partial z_b/\partial y\right)^2}$ (Hervouet 2003).

Boundary conditions for the sediment advection-diffusion equation express the exchange rate $\tilde{S}^d_{\phi,b}$ of sediments between the bed and the flow layer:

$$\tilde{S}^d_{\phi,b}\,\Delta\Sigma = \left[\tilde{q}^d_{\phi,x}\right]_b\frac{\partial z_b}{\partial x} + \left[\tilde{q}^d_{\phi,y}\right]_b\frac{\partial z_b}{\partial y} - \left[\tilde{q}^d_{\phi,z}\right]_b . \tag{8}$$

while this exchange rate is simply zero at the free surface.

Scaling and shallow flow assumption

Standard scaling analysis of equations (1)-(3) proves useful to further simplify the derivation of the depth-averaged model. If the characteristic flow depth H is assumed much smaller than the characteristic length scale L in the x-y plane, then the depth-averaged z momentum balance is shown to reduce to the hydrostatic equilibrium:

$$\frac{\partial p}{\partial z} = -\rho g \sin\theta_z \quad \Rightarrow \quad p(z) = g \sin\theta_z \int_z^{z_s} \rho \, dz' \,. \tag{9}$$

This in turn provides an explicit relationship between the pressure and other flow variables such as density and water depth.

General depth-averaged model

Integration of the three-dimensional equations (1)-(3) over the local flow depth, accounting for the boundary conditions (5)-(8), results in the following set of two-dimensional equations:

$$\frac{\partial}{\partial t}\left(h\overline{\rho}\right) + \frac{\partial}{\partial x}\left(h\overline{\rho u}\right) + \frac{\partial}{\partial y}\left(h\overline{\rho v}\right) = -\rho_\mathrm{b} r_\mathrm{b} \tag{10}$$

$$\begin{aligned} &\frac{\partial}{\partial t}\left(h\overline{\rho u}\right) + \frac{\partial}{\partial x}\left(h\overline{\rho u^2}\right) + \frac{\partial}{\partial y}\left(h\overline{\rho u v}\right) \\ &\qquad = -\frac{\partial h\overline{p}}{\partial x} - \rho_\mathrm{b} u_\mathrm{b} r_\mathrm{b} - \left[p\right]_\mathrm{b} \frac{\partial z_\mathrm{b}}{\partial x} + \frac{\partial h\overline{\sigma_x}}{\partial x} + \frac{\partial h\overline{\tau_{xy}}}{\partial y} + \tau_{\mathrm{b}x}\Delta\Sigma + h\overline{\rho} g \sin\theta_x \end{aligned} \tag{11}$$

$$\begin{aligned} &\frac{\partial}{\partial t}\left(h\overline{\rho v}\right) + \frac{\partial}{\partial x}\left(h\overline{\rho u v}\right) + \frac{\partial}{\partial y}\left(h\overline{\rho v^2}\right) \\ &\qquad = -\frac{\partial h\overline{p}}{\partial y} - \rho_\mathrm{b} v_\mathrm{b} r_\mathrm{b} - \left[p\right]_\mathrm{b} \frac{\partial z_\mathrm{b}}{\partial y} + \frac{\partial h\overline{\tau_{yx}}}{\partial x} + \frac{\partial h\overline{\sigma_y}}{\partial y} + \tau_{\mathrm{b}y}\Delta\Sigma + h\overline{\rho} g \sin\theta_y \end{aligned} \tag{12}$$

$$\begin{aligned} &\frac{\partial}{\partial t}\left(h\overline{\rho\phi}\right) + \frac{\partial}{\partial x}\left(h\overline{\rho u\phi}\right) + \frac{\partial}{\partial y}\left(h\overline{\rho v\phi}\right) \\ &\qquad = -\rho_\mathrm{b}\phi_\mathrm{b} r_\mathrm{b} - \left[\frac{\partial}{\partial x}\left(h\overline{\tilde{q}^\mathrm{d}_{\phi,x}}\right) + \frac{\partial}{\partial y}\left(h\overline{\tilde{q}^\mathrm{d}_{\phi,y}}\right)\right] + \tilde{S}^\mathrm{d}_{\phi,\mathrm{s}} - \tilde{S}^\mathrm{d}_{\phi,\mathrm{b}} + h\overline{\tilde{S}_\phi} \end{aligned} \tag{13}$$

Overbars denote depth-averaged quantities. So far, no particular velocity or concentration profile has been assumed and the set of equations holds whatever the velocity and concentration distributions across the flow layer.

Bed-load mass balance equation

Besides the flow and transport equations (10)-(13), an additional mass balance equation for the bed-load is necessary to constitute the complete morphodynamic model. As sketched in Fig. 2, two layers may be distinguished in the bed material. The lower layer consists of bed material at rest, while bed-load takes place in the upper layer. Sediment continuity in the bed-load layer is expressed by Exner equation:

$$(1-p)\frac{\partial z_\mathrm{b}}{\partial t} + \frac{\partial q_{\mathrm{b}x}}{\partial x} + \frac{\partial q_{\mathrm{b}y}}{\partial y} = -e_\mathrm{b} \tag{14}$$

Notations $q_{\mathrm{b}x}$ and $q_{\mathrm{b}y}$ denote the bed-load unit discharges along x and y respectively. The sediment flux normal to the bed $e_\mathrm{b} = E - D$ represents the net sediment exchange rate between the bed and the flow layer.

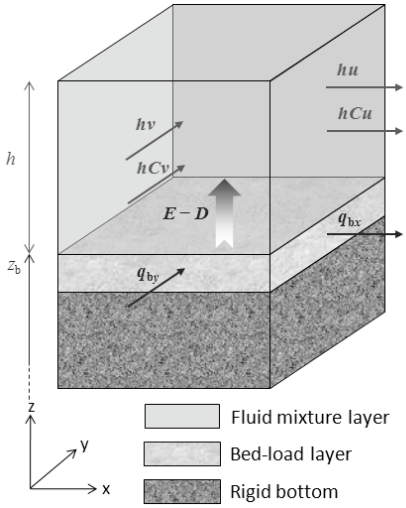

Fig. 2. Schematic configuration underlying the depth-averaged morphodynamic model.

Characteristics of flow-sediment mixtures

To derive our two-phase morphodynamic model from the general depth-averaged continuity and momentum equations (10)-(13) for the sediment-laden flow and for the dispersed phase (suspended load), adequate density, velocity and concentration profiles must be we incorporated in equations (10)-(13). For a water-sediment mixture, density and mass concentration are given by:

$$\rho = \rho_w (1 - C) + \rho_s C = \rho_w \left[1 + (s - 1) C \right] = \rho_w (1 + \Delta s C) \tag{15}$$

$$\phi = \frac{\rho_s C}{\rho} = \frac{\rho_s C}{\rho_w (1 + \Delta s C)} = \frac{sC}{1 + \Delta s C} \tag{16}$$

with $s = \rho_s / \rho_w$ the relative density of sediments and the notation Δ is defined as $\Delta s = s - 1$.
The real concentration profile is highly case-dependent and, for transient and varied flows, it may considerably deviate from computed equilibrium distributions, such as Rouse-type profiles. Therefore, we simply assume here a uniform concentration profile, which is found close to observations for highly transient flows accompanied by high transport rates. For similar reasons, the velocity profile is also simply assumed to be uniform.
We neglect the possible effects of differential advection of momentum due to a non-uniform velocity profile. Indeed, inclusion of a correction factor, so-called Boussinesq coefficient (Hervouet et al. 2003), appears unnecessary for a wide range of applications, in which the shear layer remains localized near the bed.
Based on the shallow flow assumption, the pressure distribution may be deduced from the simplified form (9) of the momentum equation along z, the direction normal to the main flow plane:

$$\frac{\partial p}{\partial z} = -\rho g \sin\theta_z = -\rho_w (1 + \Delta s C) g \sin\theta_z \,. \tag{17}$$

Assuming a uniform concentration profile along z and using the atmospheric pressure at the free surface as reference pressure, the following expressions involved in the governing equations (11)-(12) may be evaluated:

$$h\overline{p} = \rho_{\mathrm{w}}\left(1+\Delta s\overline{C}\right)g\sin\theta_z\, h^2/2 \quad \text{and} \quad p_{\mathrm{b}} = \rho_{\mathrm{w}}\left(1+\Delta s\overline{C}\right)g\sin\theta_z\, h\,. \tag{18}$$

Diffusive fluxes in the sediment advection-diffusion equation are evaluated as follows:

$$\overline{q^{\mathrm{d}}_{C,x}} = -\frac{\nu_{\mathrm{T}}}{\sigma_{\mathrm{T}}}\frac{\partial\overline{C}}{\partial x} \quad \text{and} \quad \overline{q^{\mathrm{d}}_{C,y}} = -\frac{\nu_{\mathrm{T}}}{\sigma_{\mathrm{T}}}\frac{\partial\overline{C}}{\partial y}\,, \tag{19}$$

where the Schmidt number σ_{T} accounts for the difference between eddy viscosity and turbulent diffusivity of sediments. Although a generally accepted evaluation of this parameter is still lacking (Cao and Carling 2002a), it is reported to vary between 0.8 and 1.2 and is often simply set to unity.

Governing equations for flow-sediment mixtures

Introducing the results (15)-(19) into equations (10)-(13) leads to the following formulation of the governing equations for two-phase mixtures of water and suspended sediments. The mixture continuity equation becomes:

$$\frac{\partial}{\partial t}\left[h\left(1+\Delta s\overline{C}\right)\right]+\frac{\partial}{\partial x}\left[h\left(1+\Delta s\overline{C}\right)\overline{u}\right]+\frac{\partial}{\partial y}\left[h\left(1+\Delta s\overline{C}\right)\overline{v}\right]=\left[1+\Delta s\left(1-p\right)\right]\frac{e_{\mathrm{b}}}{1-p} \tag{20}$$

whereas, using expressions (18), the mixture momentum equations may be written as:

$$\begin{aligned}&\frac{\partial}{\partial t}\left[h\left(1+\Delta s\overline{C}\right)\overline{u}\right]+\frac{\partial}{\partial x}\left[h\left(1+\Delta s\overline{C}\right)\overline{u}^2\right]+\frac{\partial}{\partial y}\left[h\left(1+\Delta s\overline{C}\right)\overline{u}\,\overline{v}\right]\\&\quad+\frac{\partial}{\partial x}\left[\left(1+\Delta s\overline{C}\right)g\sin\theta_z\frac{h^2}{2}\right]+h\left(1+\Delta s\overline{C}\right)g\sin\theta_z\frac{\partial z_{\mathrm{b}}}{\partial x}\\&\quad=\left[1+\Delta s\left(1-p\right)\right]\frac{e_{\mathrm{b}}-\left|e_{\mathrm{b}}\right|}{2\left(1-p\right)}\overline{u}\beta+\frac{\tau_{\mathrm{b}x}}{\rho_{\mathrm{w}}}\Delta\Sigma+h\left(1+\Delta s\overline{C}\right)g\sin\theta_x+\frac{1}{\rho_{\mathrm{w}}}\left(\frac{\partial h\overline{\sigma_x}}{\partial x}+\frac{\partial h\overline{\tau_{xy}}}{\partial y}\right),\end{aligned} \tag{21}$$

$$\begin{aligned}&\frac{\partial}{\partial t}\left[h\left(1+\Delta s\overline{C}\right)\overline{v}\right]+\frac{\partial}{\partial x}\left[h\left(1+\Delta s\overline{C}\right)\overline{u}\,\overline{v}\right]+\frac{\partial}{\partial y}\left[h\left(1+\Delta s\overline{C}\right)\overline{v}^2\right]\\&\quad+\frac{\partial}{\partial y}\left[\left(1+\Delta s\overline{C}\right)g\sin\theta_z\frac{h^2}{2}\right]+h\left(1+\Delta s\overline{C}\right)g\sin\theta_z\frac{\partial z_{\mathrm{b}}}{\partial y}\\&\quad=\left[1+\Delta s\left(1-p\right)\right]\frac{e_{\mathrm{b}}-\left|e_{\mathrm{b}}\right|}{2\left(1-p\right)}\overline{v}\beta+\frac{\tau_{\mathrm{b}y}}{\rho_{\mathrm{w}}}\Delta\Sigma+h\left(1+\Delta s\overline{C}\right)g\sin\theta_y+\frac{1}{\rho_{\mathrm{w}}}\left(\frac{\partial h\overline{\tau_{xy}}}{\partial x}+\frac{\partial h\overline{\sigma_y}}{\partial y}\right).\end{aligned} \tag{22}$$

Expressing the density ρ as in (15) and the mass concentration ϕ as a function of the volume concentration C according to (16), the continuity equation for the dispersed phase writes:

$$\frac{\partial}{\partial t}\left(h\overline{C}\right)+\frac{\partial}{\partial x}\left(h\overline{u}\overline{C}\right)+\frac{\partial}{\partial y}\left(h\overline{v}\overline{C}\right)=-\left[\frac{\partial}{\partial x}\left(h\frac{\nu_{\mathrm{T}}}{\sigma_{\mathrm{T}}}\frac{\partial\overline{C}}{\partial x}\right)+\frac{\partial}{\partial y}\left(h\frac{\nu_{\mathrm{T}}}{\sigma_{\mathrm{T}}}\frac{\partial\overline{C}}{\partial y}\right)\right]+e_{\mathrm{b}}. \tag{23}$$

Finally, the morphodynamic evolution is governed by Exner equation expressing the bed-load continuity as in (14):

$$\frac{\partial}{\partial t}\left[(1-p)z_\mathrm{b}\right]+\frac{\partial q_{\mathrm{b}x}}{\partial x}+\frac{\partial q_{\mathrm{b}y}}{\partial y}=-e_\mathrm{b}\,, \tag{24}$$

where $e_\mathrm{b} = E - D$ is the *net* erosion rate, evaluated as the difference between the erosion flux E (m/s) and the deposition flux D (m/s). A detailed discussion of the formulation of all terms involving the net erosion rate in (20)-(24) is given by Dewals (2006). The solid unit discharges $q_{\mathrm{b}x}$ and $q_{\mathrm{b}y}$ include both the flow-induced and the gravity-induced (slope failures) components of bed sediment transport.

Closure of the set of equations (20)-(24) requires a resistance formula to compute $\tau_{\mathrm{b}x}/\rho_\mathrm{w}$ and $\tau_{\mathrm{b}y}/\rho_\mathrm{w}$, a turbulence model, as well as an exchange model for evaluating $E - D$.

Instead of a uniform concentration profile, a piecewise uniform profile may also be assumed, leading to only slight modifications in the governing equations. Indeed, if the concentration is assumed to take a uniform value C_b for $z_\mathrm{b} \le z \le z_\mathrm{b} + h_1$ and zero above, only two changes are necessary in the equations: $h\overline{C}$ is replaced by $h_1 C_\mathrm{b}$ and the pressure term $\left(1+\Delta s\overline{C}\right)g\sin\theta_z\left(h^2/2\right)$ becomes $\left(h^2/2+\Delta s C_\mathrm{b} h_1^2/2\right)g\sin\theta_z$. Previous authors have used such approximations keeping C_b constant and computing the evolution of h_s (Fraccarollo and Capart 2002) or using appropriate empirical relations (Leal et al. 2003).

The set of governing equations (20)-(24) may be recast in the following vector form, which simplifies the formulation of the numerical scheme detailed in section 2.3:

$$\frac{\partial \mathbf{s}}{\partial t}+\frac{\partial \mathbf{f}_\mathrm{a}}{\partial x}+\frac{\partial \mathbf{f}_\mathrm{d}}{\partial x}+\mathbf{A}_{\mathrm{NC}}^{-}\frac{\partial \mathbf{s}}{\partial x}+\frac{\partial \mathbf{g}_\mathrm{a}}{\partial x}+\frac{\partial \mathbf{g}_\mathrm{d}}{\partial x}+\mathbf{B}_{\mathrm{NC}}^{-}\frac{\partial \mathbf{s}}{\partial x}=\mathbf{r} \tag{25}$$

with

$$\mathbf{s}=\left[h\left(1+\Delta s\overline{C}\right)\quad h\left(1+\Delta s\overline{C}\right)\overline{u}\quad h\left(1+\Delta s\overline{C}\right)\overline{v}\quad h\overline{C}\quad (1-p)z_\mathrm{b}\right]^\mathrm{T} \tag{26}$$

$$\mathbf{f}_\mathrm{a}=\left[h\left(1+\Delta s\overline{C}\right)\overline{u}\quad h\left(1+\Delta s\overline{C}\right)\overline{u}^2+gh^2\left(1+\Delta s\overline{C}\right)\sin\theta_z\quad h\left(1+\Delta s\overline{C}\right)\overline{u}\overline{v}\quad h\overline{u}\overline{C}\quad q_{\mathrm{b}x}\right]^\mathrm{T} \tag{27}$$

$$\mathbf{g}_\mathrm{a}=\left[h\left(1+\Delta s\overline{C}\right)\overline{v}\quad h\left(1+\Delta s\overline{C}\right)\overline{u}\overline{v}\quad h\left(1+\Delta s\overline{C}\right)\overline{v}^2+gh^2\left(1+\Delta s\overline{C}\right)\sin\theta_z\quad h\overline{v}\overline{C}\quad q_{\mathrm{b}y}\right]^\mathrm{T} \tag{28}$$

$$\mathbf{f}_\mathrm{d}=\left[0\quad \frac{h\overline{\sigma}_x}{\rho_\mathrm{w}}\quad \frac{h\overline{\tau}_{xy}}{\rho_\mathrm{w}}\quad h\frac{\nu_\mathrm{T}}{\sigma_\mathrm{T}}\frac{\partial\overline{C}}{\partial x}\quad 0\right]^\mathrm{T};\quad \mathbf{g}_\mathrm{d}=\left[0\quad \frac{h\overline{\tau}_{xy}}{\rho_\mathrm{w}}\quad \frac{h\overline{\sigma}_x}{\rho_\mathrm{w}}\quad h\frac{\nu_\mathrm{T}}{\sigma_\mathrm{T}}\frac{\partial\overline{C}}{\partial y}\quad 0\right]^\mathrm{T} \tag{29}$$

$$\mathbf{A}_{\mathrm{NC}}^{-}=\begin{pmatrix}0&0&0&0&0\\0&0&0&0&h\left(1+\Delta s\overline{C}\right)\dfrac{g\sin\theta_z}{1-p}\\0&0&0&0&0\\0&0&0&0&0\\0&0&0&0&0\end{pmatrix};\quad \mathbf{B}_{\mathrm{NC}}^{-}=\begin{pmatrix}0&0&0&0&0\\0&0&0&0&0\\0&0&0&0&h\left(1+\Delta s\overline{C}\right)\dfrac{g\sin\theta_z}{1-p}\\0&0&0&0&0\\0&0&0&0&0\end{pmatrix} \tag{30}$$

and $\mathbf{r}$ gathers all source terms.

2.3 Numerical discretization

The set of governing equations (20)-(24) is solved using a finite volume technique. Details of the time and space discretizations are provided here, together with a discussion on sequential vs. synchronous resolution procedures of the morphodynamic model.

Space and time discretization

The computation domain is discretized by means of a multiblock grid, in which each block consists in a locally Cartesian mesh. Since this multiblock structure enables refined meshes in critical areas (high gradients, complex geometry), it compensates for the lower flexibility of Cartesian grids, while keeping the benefits of regular grids in terms of order of accuracy, computation time and memory requirement.

The space discretization of the divergence form of equations (20)-(24)is performed by means of a finite volume scheme. Within each block, variable reconstruction at cells interfaces can be performed by constant or linear extrapolation, combined with a slope limiter, leading respectively to first or second order accuracy. Variables at the borders between adjacent blocks are extrapolated linearly, using additional ghost points. The value of the variables at the ghost points is evaluated from the value of the subjacent cells. Moreover, to ensure conservation properties at the border between adjacent blocks and thus to compute accurate continuity and momentum balance, fluxes related to the larger cells are computed at the level of the finer ones.

Advective fluxes are computed by a Flux Vector Splitting (FVS) method developed by the authors. According to this FVS, the upwinding direction of each term of the fluxes $\mathbf{f}_a$ and $\mathbf{g}_a$ is simply dictated by the sign of the flow velocity reconstructed at the cells interfaces. It has thus the advantage of being completely Froude independent and of facilitating a satisfactory adequacy with the discretization of the bed elevation gradient (Erpicum et al. 2010a). It can be formally expressed as follows:

$$\mathbf{f}_a^+ = \left[h\left(1+\Delta s\overline{C}\right)\overline{u} \quad h\left(1+\Delta s\overline{C}\right)\overline{u}^2 \quad h\left(1+\Delta s\overline{C}\right)\overline{uv} \quad h\overline{u}\overline{C} \quad q_{bx} \right]^T \tag{31}$$

$$\mathbf{f}_a^- = \left[0 \quad gh^2\left(1+\Delta s\overline{C}\right)\sin\theta_z \quad 0 \quad 0 \quad 0 \right]^T \tag{32}$$

$$\mathbf{g}_a^+ = \left[h\left(1+\Delta s\overline{C}\right)\overline{v} \quad h\left(1+\Delta s\overline{C}\right)\overline{uv} \quad h\left(1+\Delta s\overline{C}\right)\overline{v}^2 \quad h\overline{v}\overline{C} \quad q_{by} \right]^T \tag{33}$$

$$\mathbf{g}_a^- = \left[h\left(1+\Delta s\overline{C}\right)\overline{v} \quad h\left(1+\Delta s\overline{C}\right)\overline{uv} \quad h\left(1+\Delta s\overline{C}\right)\overline{v}^2 + gh^2\left(1+\Delta s\overline{C}\right)\sin\theta_z \quad h\overline{v}\overline{C} \quad q_{by} \right]^T \tag{34}$$

where the exponents $+$ and $-$ refer to, respectively, an upstream and a downstream evaluation of the corresponding terms. A Von Neumann stability analysis has demonstrated that this FVS leads to a stable spatial discretization of the terms $\partial\mathbf{f}_a/\partial x$ and $\partial\mathbf{g}_a/\partial y$ in (25) (Dewals 2006). Due to their diffusive nature, the fluxes $\mathbf{f}_d$ and $\mathbf{g}_d$ are legitimately evaluated by means of a centred scheme.

Since the model is applied to compute steady-state solutions, the time integration is performed by means of a three-step first order accurate Runge-Kutta algorithm, providing adequate dissipation in time. For stability reasons, the time step is constrained by the Courant–Friedrichs–Levy (CFL) condition. A semi-implicit treatment of the bottom friction term (3) is used, without requiring additional computational cost.

Synchronous vs. sequential resolution procedure

A challenging issue in sediment transport modelling is the need to handle accurately and efficiently the wide range of time scales involved in the relevant phenomena. Indeed the time scales of interest extend from a few seconds or minutes (e.g. slope failures or rapid scouring) to periods as long as years or decades (long term sedimentation). Therefore, specific numerical modelling tools must be combined to handle reliably and at an acceptable computational cost the processes characterized by time scales spanning over such a wide range. To this end, our modelling system enables to solve the sub-models for flow and for sediment transport as well as morphodynamics in either a synchronous or a sequential numerical procedure.

In the former case, submodels for flow, sediment transport and morphodynamics are all updated by one time step simultaneously. This turns out to be the only appropriate procedure for handling "transcritical" flows, in the range approximately given by $0.6 \leq Fr \leq 1.4$ as detailed by Dewals et al. (2008a). We have successfully used this resolution strategy for modelling transient geomorphic flows induced by dam break and dam breaching (Dewals et al. 2002a; Dewals et al. 2002b; Dewals et al. 2002c), as well as flushing operations in silted reservoirs (Dewals et al. 2004; Dewals et al. 2008a; Dewals et al. 2010b).

In contrast, the widely used sequential procedure is based on a quasi-steady description of the flow, which is assumed not to evolve during each time step of the morphodynamic model. This resolution strategy is substantiated by the significant difference usually prevailing in-between flow and morphodynamic characteristic time scales. In sub- and super-critical gradually-varied flows, the flow itself generally adapts much faster than the morphology: morphological changes in response to flow changes take much longer than the time required for the flow to adapt to a new bed geometry. Nonetheless, if inappropriately used, the sequential resolution may degrade both the accuracy and stability of the solution of the set of governing equations for flow, sediment transport and bed evolution (Cao et al. 2002). We have applied this resolution procedure for predicting long term reservoir sedimentation (Dewals et al. 2004; Dewals et al. 2008a), leading to a dramatic reduction in computational time compared to the purely synchronous resolution. Using the so-called morphological factor may also help to save computational resources within the synchronous resolution procedure (Kleinhans et al. 2008; van Rijn et al. 2007).

Validated numerical model and other main features

The herein described model constitutes a part of the modelling system “WOLF”, developed at the University of Liege. WOLF includes a set of complementary and interconnected modules for simulating a wide range of free surface flows, involving process-oriented rainfall-runoff modelling, 1D, 2DH, 2DV and 3D hydrodynamics, sediment or pollutant transport, air entrainment, as well as an optimisation tool based on Genetic Algorithms.

Validity and efficiency of the model has already been proved for numerous applications (Dewals et al. 2008b; Erpicum et al. 2009; Kerger et al. 2010a), including inundation mapping (Ernst et al. 2010; Erpicum et al. 2010a; Khuat Duy et al. 2010), dam break and dam breaching simulations (Dewals et al. 2010a; Erpicum et al. 2010b; Roger et al. 2009) as well as morphodynamic modelling (Dewals et al. 2002a; Dewals et al. 2002b; Dewals et al. 2002c; Dewals et al. 2004; Dewals et al. 2008a; Dewals et al. 2010b).

Other functionalities of WOLF include the use of moment of momentum equations (Dewals 2006), the application of the cut-cell method, as well as computations considering bottom curvature effects by means of curvilinear coordinates in the vertical plane (Dewals et al. 2006).

A user-friendly interface, entirely designed and implemented by the authors, makes the pre- and post-processing operations particularly convenient. Import and export operations are easily feasible from and to various classical GIS tools. Several layers can be handled to make the analysis of various data sets easier such as topography, land use, vegetation density, hydrodynamic fields...

3. Sediment routing on partially non-alluvial beds

In depth-averaged flow models, the flow depth is computed numerically as a result of time integration of the continuity equation, usually using an explicit algorithm. Therefore, it is well known that, on drying cells, the computed value may be found negative, which is physically unsound. This issue may be handled by properly modifying computed depths, while keeping the mass conservation still verified. A number of models addressing somehow this issue have been reported (Begnudelli and Sanders 2007 ; Gourgue et al. 2009), but without necessarily achieving exact mass conservation. Numerical schemes consistently keeping the computed water depth positive exist (Audusse et al. 2004), but they do not address sediment transport issues, particularly on partly rigid beds.
A very similar difficulty arises when dealing with sediment transport and morphodynamic modelling on partly non-alluvial beds, where the nature of the soil makes erosion impossible in some locations (bedrock, armoured layer, concrete structure). In such cases, when the computed value for bottom elevation becomes lower than the level of the top of the non-erodible layer, the computed value also needs to be modified without compromising the global mass balance of sediments.
This numerical treatment of sediment routing on partly non-alluvial beds remains complex, since erosion must be prevented from extending deeper than the level of the non-alluvial bed whereas neither deposition nor sediment discharge should be constraint.
Details on this computational issue are hardly available in literature. Some existing modelling procedures for bed-load transport over non-erodible layers assume, for instance, a progressive decrease of the bed-load transport when sediment level becomes close to the fixed bottom (Struiksma 1999). Nonetheless, there remains a lack of transparency on how many existing models deal with sediment transport on non-alluvial beds and, especially, on possible mass conservation errors introduced by the treatment.
In this section, we recall the approach suggested by Struiksma (1999); then we introduce our original procedure and finally we discuss their relative performance based on three test cases, among which one is conceptual while the others rely on experimental data.

3.1 Existing vs. original treatment of non-alluvial beds

Struiksma approach

A method to solve the problem of sediment routing on partially rigid bottoms was proposed by Struiksma (1999). It consists in modifying the customary deterministic bed-load transport formula $q_{b,c}(h,u,v)$ (such as Meyer-Peter Müller, Schoklitsch, Bagnold, power law ...) as follows:

$$q_b = \psi\left(\frac{\delta(x)}{\delta_a(h)}\right) q_{b,c}(h,u,v)\,, \tag{35}$$

where δ_a is the maximum thickness of alluvium for which the non-erodible layer still affects the sediment transport, δ is the actual thickness of alluvium (Fig. 3) and ψ is a function of δ/δ_a which limits the bed-load transport flux due to the proximity of non-erodible areas. The thickness value δ_a is reported to be approximately equal to half of the bed form height. For $\delta = 0$, sediment transport is not possible anymore ($\psi = 0$); while for $\delta = \delta_a$, the presence of the non erodible layer is considered to have no influence on the bed-load discharge ($\psi = 1$). Thus, the function ψ monotonously increases between these two extreme values. The modified bed-load transport formula is then used in the Exner equation. A disadvantage of this method may rise from some lack of generality because δ_a remains a calibration parameter which may vary depending on topography, water depth, flow regime...

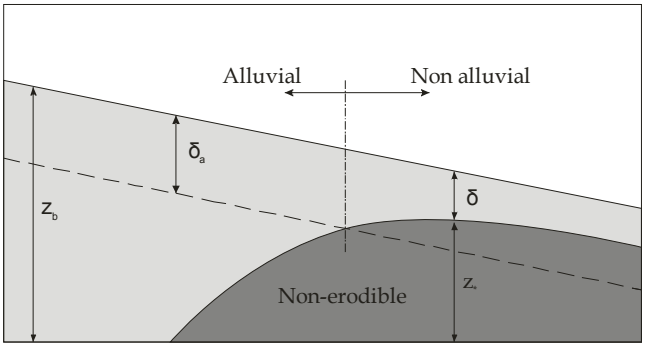

Fig. 3. Definition of the concept of alluvial and non-alluvial areas

Original procedure

Our original method introduced here uses the depth-averaged two-phase flow model presented in section 2. We focus here on bed-load transport on a partially non-alluvial bottom. Thus, the concentration is set to zero in equation (23) and the set of equations (20)-(24) becomes:

$$\frac{\partial h}{\partial t} + \frac{\partial h\overline{u}}{\partial x} + \frac{\partial h\overline{v}}{\partial y} = 0 \tag{36}$$

$$\frac{\partial h\overline{u}}{\partial t} + \frac{\partial h\overline{u}^2}{\partial x} + \frac{\partial h\overline{u}\,\overline{v}}{\partial y} + \frac{\partial}{\partial x}\left(g\sin\theta_z \frac{h^2}{2}\right) + hg\sin\theta_z \frac{\partial z_b}{\partial x} = \frac{\tau_{bx}}{\rho}\Delta\Sigma + hg\sin\theta_x + \frac{1}{\rho}\left(\frac{\partial h\overline{\sigma_x}}{\partial x} + \frac{\partial h\overline{\tau_{xy}}}{\partial y}\right), \tag{37}$$

$$\frac{\partial h\overline{v}}{\partial t} + \frac{\partial h\overline{u}\,\overline{v}}{\partial x} + \frac{\partial h\overline{v}^2}{\partial y} + \frac{\partial}{\partial y}\left(g\sin\theta_z \frac{h^2}{2}\right) + hg\sin\theta_z \frac{\partial z_b}{\partial y} = \frac{\tau_{by}}{\rho}\Delta\Sigma + hg\sin\theta_y + \frac{1}{\rho}\left(\frac{\partial h\overline{\tau_{xy}}}{\partial x} + \frac{\partial h\overline{\sigma_y}}{\partial y}\right), \tag{38}$$

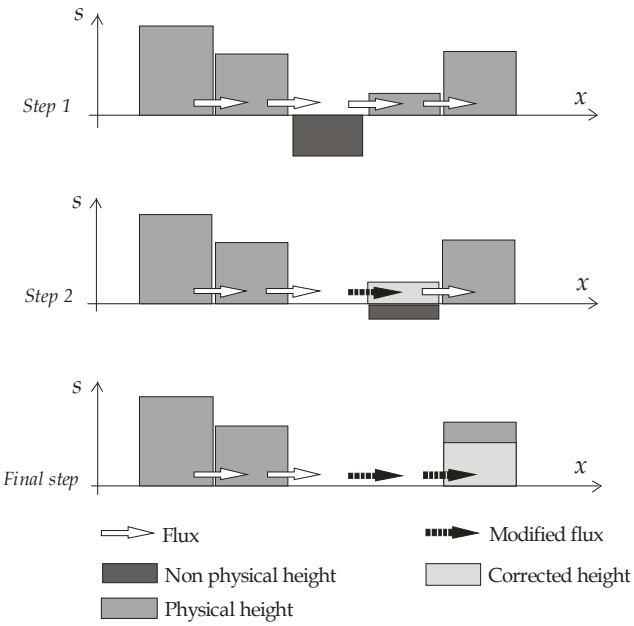

Fig. 4. Three-step procedure

$$\frac{\partial}{\partial t}\left[(1-p)z_b\right]+\frac{\partial q_{bx}}{\partial x}+\frac{\partial q_{by}}{\partial y}=0\,. \tag{39}$$

As emphasized at the beginning of this section, the difficulties in the numerical treatment of drying cells and non-alluvial beds are highly similar. This is notably due to the formal similarity in the mathematical formulation of Exner equation (39) and of the flow continuity equation (36). Our original approach consists thus in developing a single procedure to correct in a similar way the non-physical sediment level and flow depth. The general mathematical form for the continuity equations (i.e. continuity equation for the mixture and Exner equation for bed-load) can be written as:

$$\frac{\partial s}{\partial t}+\frac{\partial f_1}{\partial x}+\frac{\partial f_2}{\partial y}=0 \tag{40}$$

where s can be the sediment level or the water depth; f_1 and f_2 are fluxes in the two directions (sediment bed-load unit discharge or flow unit discharge). Thanks to an efficient iterative resolution of the continuity equations, correct mass and momentum conservation are ensured using a three-step procedure at each time step:

- Equation (40) is evaluated (step 1 in Fig. 4).
- Algorithm detects whether the current height as given by Equation (40) is under the level of the reference height (zero water depth or fixed bottom level). Thus, it highlights the occurrence of computed non physical configurations such as negative water depth and erosion of non-erodible bottom. Then, in cells with non physical configurations, the

outflow discharge is reduced (step 2 in Fig. 4 ; dashed arrow) such that the computed height becomes strictly equal to the reference height ($f_{1,new}^{out} = f_1^{out}.\alpha$ and $f_{2,new}^{out} = f_2^{out}.\alpha$).

- Since these flux corrections may in turn induce another non physical configuration in neighbouring cells, the two points above are repeated iteratively. At the end, this leads to a configuration in which the heights are all in their physical range, as shown in final step in Fig. 4.

3.2 Model verification

The depth-averaged two-phase flow model combined with the algorithm of flow depth and sediment level correction has been verified using several benchmarks leading to configurations with negative water depth or sediment transport over non-erodible bottoms. After a clear-water flow standard benchmark (dam break flow travelling on a sharp bump), scouring of a trench initially filled with sediments as well as the migration of a trench passing over a fixed bump have been tested.

Dam break flow travelling on a sharp bump

Water at rest is assumed to be initially stored in a prismatic reservoir 15.5 m long, 0.75 m wide and 0.75 m high (Fig. 5). In the downstream part of the channel, a sharp symmetric bump is located 13 m downstream of the dam, followed by water at rest with a maximum depth of 0.15 m. The bump is made of two 13.33 % slopes, with a maximum height of 0.4 m. The computational domain is a 38-m long straight channel limited by two fixed walls (Fig. 5). At time $t = 0$ *s*, the dam is assumed to break, releasing the previously stored water which flows downstream leading eventually to wetting and subsequently drying of the bump crest.

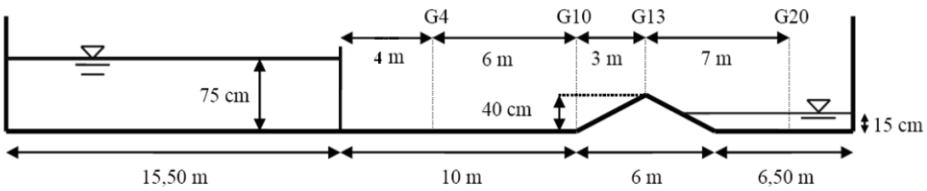

Fig. 5. Sketch of the experimental setup and location of the gauges.

The numerical simulation was carried out with a cell size of 0.1 m and a Manning coefficient equal to 0.005 s/m$^{1/3}$. The computed results are compared with experimental results (Morris and Galland 2000) obtained at four gauges (G4, G10, G13, G20 in Fig. 5). This experiment has been repeated twice (Experimental 1 and 2 in Fig. 6).

Fig. 6 shows that the computed depth remains always positive and that the numerical predictions match measurements throughout the considered time range. In particular, the reflexion wave reaching gauge G4 after approximately 13.5 seconds in the experiments is accurately reproduced in the numerical simulation; both in terms of wave velocity and wave height. The slightly noticeable temporal shift between experimental data and computed results may be attributed to the non-instantaneous collapse of the dam in the experimental setup. Finally, mass is conserved in the simulations, as verified by comparing water volumes between initial and final times: $\Delta V_{\text{water}} \approx 6 \times 10^{-10}$ m^3/m.

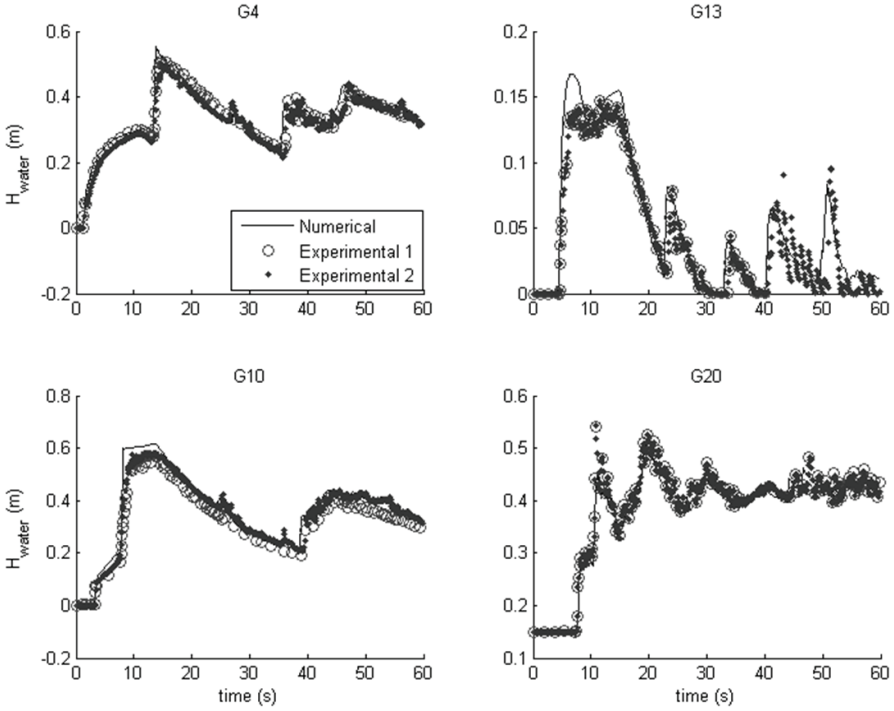

Fig. 6. Evolution of the water depth at gauges.

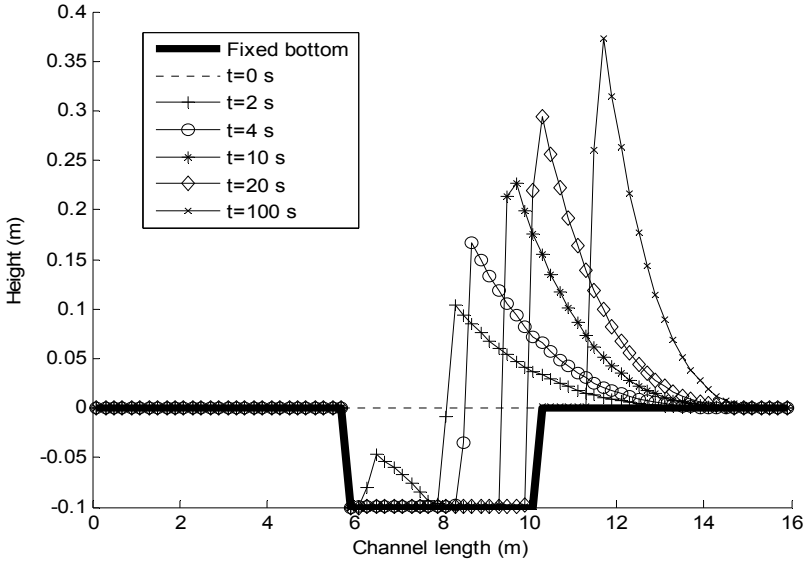

Fig. 7. Bed evolution in the hypothetical test case.

Scour of a trench initially filled with sediments

A prismatic channel is considered here, with a 1.1 m-wide rectangular cross section. The length of the channel is 16 m. The cell size used in the longitudinal direction is 0.2 m. The rigid bottom corresponds to the level zero throughout the channel, except in a 4.5 m-long trench located at mid-length of the channel, where the rigid bottom elevation is set to - 0.1 m (Hervouet et al. 2003). This trench is filled with sediments up to the level zero (see Fig. 7). In this hypothetical test case, the flow conditions are kept artificially constant in time. The flow discharge is assumed to increase linearly from 0 to 10 m²/s between the abscissa x = 0m and the abscissa x = 8m; and decrease linearly from 10 to 0 m²/s between the abscissa x = 8m and the abscissa x = 16m. The water depth is set everywhere equal to 2 m. The Manning coefficient is taken equal to $n = 0.04\ \mathrm{s/m^{1/3}}$. The Engelund-Hansen bed-load transport formula is used in this case, in which the grain diameter is assumed equal to d_{50} = 0.3 mm, the specific gravity of sediments is s = 2.65 and the porosity of bed material is p = 0.375.
The computed time evolution of the bed profile is shown in Fig. 7. After 100 seconds, the bed profile does not move anymore. Although no direct comparison data are available, the model is found to perform satisfactorily since the computed bed level always remains above the level of the non erodible bottom and no mass conservation error is found in the computational results.

Evolution of a trench over a fixed bump

This test case considers the evolution of a trench passing over a non erodible bump. The length of the straight channel is 11.5 m and its width is 0.2 m. A bump is located in the middle of the domain while an approximately 0.04 m deep and 2 m long trench is excavated in the alluvial bed upstream. The grain diameter is taken equal to 0.45 mm. The cell size is 0.1 m. The computed bed-load transport law is assumed to be a power function of the water velocity: $q_b = m\,u^5$. The hydrodynamic and morphodynamic conditions are detailed in Table 1. Coefficient m in Table 1 was used as a tuning parameter to reproduce the propagation of the front of the trench over the first two meters in the upstream section (Struiksma 1999). Two experiments were carried out. In Test n°1, the thickness of alluvium on the bump is small while in test n°2, the thickness is zero. We can also observe that the two fixed bumps and the two trenches have different shapes.
Comparisons between numerical and experimental results are shown in Fig. 8. For both test-cases, experimental data are scattered but the overall agreement with numerical predictions is found satisfactory. Our new algorithm performs well since the sediment level is never computed under the level of non erodible bottom, with a mass conservation error of the order of the floating-point accuracy.

Quantity	Unit	T1	T2
Discharge	l/s	9.2	9.2
Mean water depth	m	0.106	0.106
Sediment transport (including pores)	l/h	4.0	4.4
Coefficient of sediment transport formula (m)	$10^{-4}\ \mathrm{s^4/m^3}$	3.6	4.0
Water surface slope	mm/m	1.75	1.75
Chézy coefficient	$\mathrm{m^{1/2}/s}$	31.8	31.8

Table 1. Hydrodynamic and morphodynamic conditions for two tests T1 and T2.

Computations however overpredict erosion depth downstream of the non erodible bump. This may result from the simplified transport capacity formula used, accounting neither for an explicit threshold for transport inception nor for gravity-induced sediment transport. Vertical accelerations might also play a part in this region. Results of T1 and T2 also reveal that the computed sediment level on the bump is underpredicted. The deeper sediment layer found experimentally may result from the medium gravels used to build the bump (non erodible under considered hydraulic conditions) leading to a high bed roughness.

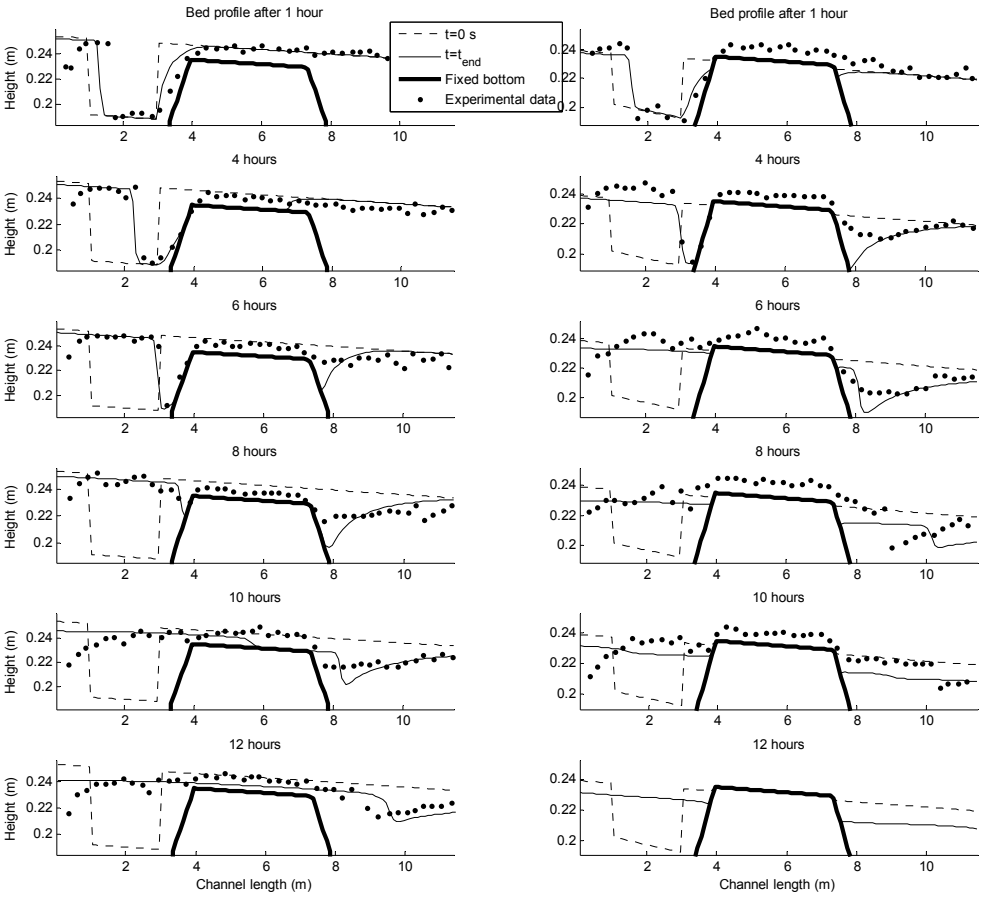

Fig. 8. Time evolution of the longitudinal bed profiles (T1, left and T2, right)

4. Application of the two-phase flow model for hyperconcentrated flows

The two-phase flow model for fluid-sediment mixtures presented in section 2 has also been used to study hyperconcentrated flows, including granular flows induced by mass failures or collapse of tailing dams on a rigid basal surface. Hyperconcentrated flows exhibit non-Newtonian behaviour and shear stress may highly depend on the concentration, properties

and dimensions of the solid particles. Two different rheological models, involving both a yield stress, are investigated, namely Bingham and frictional fluid models. In the former case, also referred to as linear viscoplastic model, once the yield stress is exceeded, the shear stress is proportional to the shear rate like in viscous flows. In the later model, yield stress depends on the pore pressure following a Coulomb-type friction law.
This section focuses first on the necessary rheological models (subsection 4.1), including their appropriate formulation for inclusion into a depth-averaged flow model. Next, the set of governing equations is recast and the numerical treatment of the yield stress is discussed (subsection 4.2). The model has eventually been validated by comparisons with analytical solutions, previous numerical results and field observations, as detailed in subsection 4.3.

4.1 Rheological models for hyperconcentrated flows

In contrast with flows generally encountered in fluvial hydraulics, dominant stresses in hyperconcentrated flows usually stem not from turbulence but mainly from collisional and frictional interactions between particles. Generalized rheological fluid models are presented hereafter, both in their 3D formulation and adapted for depth-averaged modelling.

General formulation

We first briefly introduce examples of rheological models in the particular case of a simple shear flow, and then we address general three-dimensional configurations.
When a Newtonian fluid undergoes simple shear, the internal shear stress (τ) evolves linearly with the shear rate ($\dot{\gamma} = du/dz$): $\tau = \mu\, du/dz$, where μ denotes the dynamic viscosity of the fluid. Contrarily, shear stress in non-Newtonian fluids evolves non-linearly with the shear rate. Besides, the fluid may additionally be characterized by a yield stress τ_0 (Fig. 9), below which the fluid does not move, despite the application of shear stress. Bingham model is an example of yield stress fluid model, with shear stress evolving linearly as a function of the shear rate beyond the threshold (linear visco-plastic model). This corresponds to a particular case of the more general Herschel-Bulkley formulation (Fig. 9).

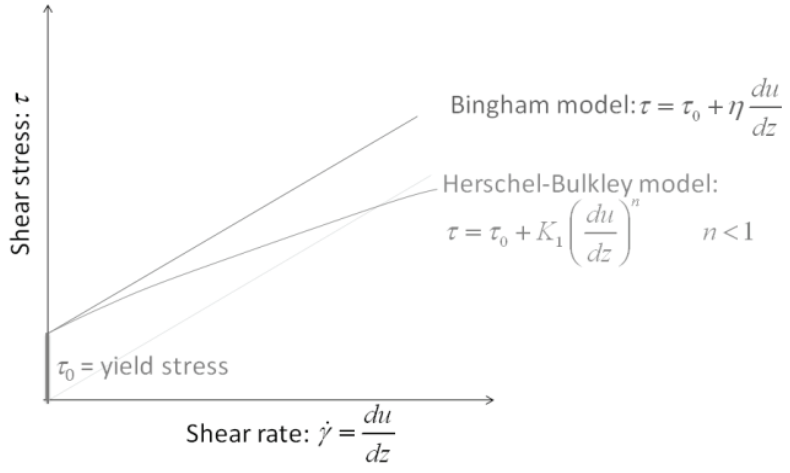

Fig. 9. Shear stress as a function of shear rate for yield stress fluids.

More generally, a rheological fluid model takes the following tensor form:

$$\boldsymbol{\sigma} = -p\mathbf{I} + \mathbf{F}(\mathbf{D}) \tag{41}$$

with $\boldsymbol{\sigma}$ the stress tensor within the fluid, p the pressure, $\mathbf{D}$ the shear rate tensor, and $\mathbf{F}$ a function to be specified depending upon the characteristics of the water-sediment mixture. The shear rate tensor is defined as:

$$D_{ij} = \frac{1}{2}\left(\frac{\partial u_i}{\partial x_j} + \frac{\partial u_j}{\partial x_i}\right) \quad \text{with} \quad i, j = x, y, z, \tag{42}$$

where x_i and u_i respectively designate spatial coordinates and velocity components.
A standard simplification for isotropic and incompressible fluids consists in specifying the general functional relationship $\mathbf{F}$ in the form of a scalar function ϕ_1 (Quecedo et al. 2004), depending only on the second invariant of the shear rate ($I_{2,\mathbf{D}}$), the first being zero as a result of the fluid incompressibility ($I_{1,\mathbf{D}} = \text{tr}\,\mathbf{D} = 0$):

$$\boldsymbol{\sigma} = -p\mathbf{I} + \phi_1\left(I_{2,\mathbf{D}}\right)\mathbf{D} \quad \text{with} \quad I_{2,\mathbf{D}} = \frac{1}{2}\text{tr}\left(\mathbf{D}^2\right). \tag{43}$$

Generally speaking, the function depends upon multiple factors, such as solid concentration, possible cohesive effects, pore pressures… The Herschel-Bulkley model (non-linear viscoplastic model) is a specific case where the function involves three parameters: yield stress τ_0, dynamic viscosity μ, and the Herschel Bulkley exponent n ($n \leq 1$):

$$\boldsymbol{\sigma} = -p\mathbf{I} + \left(\frac{\tau_0}{\sqrt{I_{2,\mathbf{D}}}} + 2\mu\left|4I_{2,\mathbf{D}}\right|^{\frac{n-1}{2}}\right)\mathbf{D} \tag{44}$$

and can in turn be particularized by choosing $n = 1$ to obtain the linear viscoplastic model:

$$\boldsymbol{\sigma} = -p\mathbf{I} + \left(\frac{\tau_0}{\sqrt{I_{2,\mathbf{D}}}} + 2\mu\right)\mathbf{D}. \tag{45}$$

Also referred to as Bingham fluid model, it involves only two parameters, assumed constant: viscosity μ and yield stress τ_0. In particular, models (44) and (45) have been applied to simulate, respectively, debris flows (e.g. Kaitna and Rickenmann 2007) and mudflows (e.g. Laigle and Coussot 1997), but also waste dump failures (e.g. Jeyapalan et al. 1983...).

Depth-averaged formulations for Bingham fluids

Similarly to all standard hydraulic resistance formulae developed for uniform flows, the depth-averaged formulation of the Bingham model is derived here assuming simple shear flow, consistently with Pastor et al. (2004).
Following notations from Fig. 1, the velocity field in a simple shear flow may be written:

$$u = U(z)\cos\alpha \qquad v = U(z)\sin\alpha \qquad w = 0 \tag{46}$$

where α represents the angle of the flow direction with respect to x- axis. Accounting for this particular velocity field, definition (42) enables to write out in full the shear rate tensor:

$$\mathbf{D} = \begin{pmatrix} 0 & 0 & \frac{1}{2}\frac{dU}{dz}\cos\alpha \\ 0 & 0 & \frac{1}{2}\frac{dU}{dz}\sin\alpha \\ \frac{1}{2}\frac{dU}{dz}\cos\alpha & \frac{1}{2}\frac{dU}{dz}\sin\alpha & 0 \end{pmatrix} \tag{47}$$

as well as its second invariant:

$$I_{2,\mathbf{D}} = \frac{1}{2}\mathrm{tr}\left(\mathbf{D}^2\right) = \frac{1}{4}\left(\frac{dU}{dz}\right)^2 . \tag{48}$$

Direct application of the rheological model (45) provides the stress tensor:

$$\boldsymbol{\sigma} = -p\mathbf{I} + \left(\frac{\tau_0}{\frac{1}{2}\frac{dU}{dz}} + 2\mu\right) = \begin{pmatrix} -p & 0 & \left(\tau_0 + \mu\frac{dU}{dz}\right)\cos\alpha \\ 0 & -p & \left(\tau_0 + \mu\frac{dU}{dz}\right)\sin\alpha \\ \left(\tau_0 + \mu\frac{dU}{dz}\right)\cos\alpha & \left(\tau_0 + \mu\frac{dU}{dz}\right)\sin\alpha & -p \end{pmatrix} \tag{49}$$

The depth-averaged flow model used hereafter (subsection 4.2) involves the following expressions, derived from the deviatoric part $\boldsymbol{\sigma}'$ of the stress tensor:

- depth-averaged normal stresses $\overline{\sigma'_{xx}}$ and $\overline{\sigma'_{yy}}$, as well as shear stress $\overline{\sigma'_{xy}}$;
- components τ_{bx} and τ_{by} of the bed shear stress $\boldsymbol{\tau}_b$, obtained from: $\boldsymbol{\tau}_b = \boldsymbol{\sigma} \cdot \mathbf{n}$.

The deviatoric part $\boldsymbol{\sigma}'$ of the stress tensor is defined by: $\boldsymbol{\sigma} = -p\,\mathbf{I} + \boldsymbol{\sigma}'$.

In the particular case of simple shear flow on a plane ($\mathbf{n} = [0\ 0\ 1]^T$), relation (49) leads to the following results:

- depth-averaged stresses are equal to zero: $\overline{\sigma'_{xx}} = \overline{\sigma'_{yy}} = \overline{\sigma'_{xy}} = 0$,
- bed shear stress is given by:

$$\tau_b = \tau_0 + \mu\left.\frac{dU}{dz}\right|_{z_b} . \tag{50}$$

This latter result, in particular dU/dz, must be expressed as a function of depth-averaged velocity, the primitive unknown of the depth-averaged model. To this end, integrating twice (50) over the flow depth, enables to obtain successively the velocity profile and the depth-averaged velocity, as detailed below.

In a simple shear flow, shear stress within the fluid varies linearly with depth:

$$\tau(z) = \tau_b\left(1 - \frac{z - z_b}{h}\right). \tag{51}$$

Consequently, two flow layers may be distinguished:

- the lower layer: $z \le z_b + h\,(1-\tau_0/\tau_b)$, in which shear stress exceeds yield stress τ_0 and a velocity profile develops,

- the upper layer: $z > z_b + h\,(1-\tau_0/\tau_b)$, where stress remains below the yield stress, so that the fluid moves like a rigid body.

Integrating first the following combination of relations (50) and (51):

$$\tau_b\left(1-\frac{z-z_b}{h}\right)=\tau_0+\mu\frac{dU}{dz} \quad \Leftrightarrow \quad \frac{dU}{dz}=\frac{\tau_b-\tau_0}{\mu}-\frac{\tau_b}{\mu}\frac{z-z_b}{h}, \tag{52}$$

leads to:

$$\begin{aligned} U &= \frac{\tau_b-\tau_0}{\mu}(z-z_b)-\frac{\tau_b}{\mu}\frac{(z-z_b)^2}{2h} && \text{for} \quad z \le z_b+h\left(1-\frac{\tau_0}{\tau_b}\right) \\ U &= \frac{\tau_b h}{2\mu}\left(1-\frac{\tau_0}{\tau_b}\right)^2 && \text{for} \quad z > z_b+h\left(1-\frac{\tau_0}{\tau_b}\right) \end{aligned}. \tag{53}$$

The depth-averaged velocity may subsequently be deduced from (53):

$$\overline{u}=\frac{\tau_b h}{2\mu}\int_0^{\frac{z_0-z_b}{h}}\left[2\left(1-\frac{\tau_0}{\tau_b}\right)\eta-\eta^2\right]d\eta+\frac{\tau_b h}{2\mu}\int_{\frac{z_0-z_b}{h}}^{1}\left(1-\frac{\tau_0}{\tau_b}\right)^2 d\eta \quad \text{with } z_0=z_b+h\left(1-\frac{\tau_0}{\tau_b}\right). \tag{54}$$

which eventually leads to the following relationship between bed shear stress τ_b and depth-average velocity $\overline{u}$:

$$\xi^3-(3+a)\xi+2=0 \quad \text{with } \xi=\frac{\tau_0}{\tau_b} \quad \text{and } a=\frac{6\mu\overline{u}}{h\tau_0}. \tag{55}$$

In this depth-averaged formulation of Bingham rheological model, bed shear stress is evaluated numerically from the root of a third order polynomial, using a Newton-Raphson procedure. Indeed, no convenient analytical solution may be found since it corresponds to a *casus irreducibilis* according to Cardano's formulae (Quecedo et al. 2004).

The Newton-Raphson iterative process is made as effective as possible by appropriately choosing the first iterate as the root between 0 and 1 of the following second degree polynomial (Pastor et al. 2004):

$$\frac{3}{2}\xi^2-\left(\frac{114}{32}+a\right)\xi+\frac{65}{32}=0, \tag{56}$$

which constitutes the best possible approximation of polynomial (55).

The Bingham model applies if variations in pore pressure remain low, which is verified in two extreme cases: either high permeability of the mixture (pore pressures dissipate fast due to a long runout time compared to the consolidation time) or low permeability of the mixture (pore pressures hardly vary during runout).

Depth-averaged formulations for frictional fluids

Compared to the Bingham model, in the pure frictional fluid model the viscous term cancels ($\mu = 0$) and the yield stress depends on effective pressure in the material through a Mohr-Coulomb type relation:

$$\tau_0 = p' \tan\phi' = \left(p - p_{\mathrm{w}}\right)\tan\phi' \tag{57}$$

where p' denotes effective pressure, p_{w} pore-pressure and ϕ' the effective friction angle. Hence relation (57) directly provides the bed shear stress, with no double integration being required, given that neither mixture velocity nor velocity gradients intervene directly in the expression:

$$\tau_{\mathrm{b}} = p'_{\mathrm{b}} \tan\phi' = \left(p_{\mathrm{b}} - p_{\mathrm{w,b}}\right)\tan\phi' . \tag{58}$$

The frictional fluid model may be combined with a simple consolidation model (Hutchinson 1986), applying an exponential decrease in pore-pressure over time:

$$\tau_0 = p'_{\mathrm{b}} \tan\phi' = p_{\mathrm{b}}\left(1 - r_u^0\, \mathrm{e}^{-\frac{t}{T_c}}\right)\tan\phi' = \rho g h\left(1 - r_u^0\, \mathrm{e}^{-\frac{t}{T_c}}\right)\tan\phi' , \tag{59}$$

where r_u^0 represents the ratio between pore-pressure and initial pressure and T_c represents the characteristic consolidation time (Hungr 1995), given by:

$$T_c = \frac{4h_s^2}{\pi^2 c_v} \qquad \text{with } c_v = \frac{k}{m_v \gamma} , \tag{60}$$

with c_v, k and m_v denoting, respectively, the consolidation coefficient, the permeability of the material and the compressibility coefficient. The frictional fluid model has been used notably to simulate waste dump failures (Pastor et al. 2002).

4.2 Governing equations

We present here a particularized form of model (20)-(22) suitable for simulating hyperconcentrated flows on rigid basal surfaces. Numerical implementation of rheological models involving a yield stress is also detailed.

Depth-averaged two-phase model for hyperconcentrated flows

Water density ρ_{w}, solid density ρ_{s} and solid fraction C are assumed constant; so that the continuity equation (20) becomes simply:

$$\frac{\partial h}{\partial t} + \frac{\partial h\overline{u}}{\partial x} + \frac{\partial h\overline{v}}{\partial y} = 0 , \tag{61}$$

in which the net erosion rate e_{b} has been set to zero since the basal surface is assumed non-erodible.

Similarly, momentum equations become:

$$\frac{\partial h\overline{u}}{\partial t} + \frac{\partial h\overline{u}^2}{\partial x} + \frac{\partial h\overline{u}\,\overline{v}}{\partial y} + \frac{\partial}{\partial x}\left(g\sin\theta_z \frac{h^2}{2}\right) + hg\sin\theta_z \frac{\partial z_{\mathrm{b}}}{\partial x} = \frac{\tau_{\mathrm{bx}}}{\rho_{\mathrm{m}}}\Delta\Sigma + hg\sin\theta_x , \tag{62}$$

$$\frac{\partial h\overline{v}}{\partial t} + \frac{\partial h\overline{u}\,\overline{v}}{\partial x} + \frac{\partial h\overline{v}^2}{\partial y} + \frac{\partial}{\partial y}\left(g\sin\theta_z \frac{h^2}{2}\right) + hg\sin\theta_z \frac{\partial z_{\mathrm{b}}}{\partial y} = \frac{\tau_{\mathrm{by}}}{\rho_{\mathrm{m}}}\Delta\Sigma + hg\sin\theta_y . \tag{63}$$

where the mixture density $\rho_m = \rho_w\left(1+\Delta s\bar{C}\right)$ has been introduced. Terms involving depth-averaged stresses have all been lumped into the flow resistance terms involving τ_b.

Numerical treatment of the yield stress

If a kinematic or diffusive wave model was used, the yield stress could be treated in a straightforward way through the algebraic relation providing velocity: when the yield stress exceeds the bed or surface gradient, velocity remains zero.
In contrast, in the case of a dynamic wave model such as used here, velocity components are evaluated from the numerical integration of partial differential equations and the accounting for the yield behaviour of the material is less straightforward, in particular in multidirectional configurations.
The main point in the numerical treatment of the yield stress consists in preventing this yield stress to cause velocity reversal, whereas such a reversal should not be prevented if it results from the action of other contributions in the equations such as adverse topographic slope. More precisely, evaluation of velocity components at each time-step is split into three stages:

1. firstly, a first velocity predictor $\mathbf{u}_{w/o}$ is evaluated without taking into account the flow resistance terms (including yield stress)
2. subsequently, a second predictor $\mathbf{u}_w$ is evaluated by resolving the complete equations (62) and (63), including the flow resistance terms.
3. finally, the value of the velocity finally retained depends on the relative position of vectors $\mathbf{u}_{w/o}$ and $\mathbf{u}_w$:
   a. if their scalar product is positive, the effect of the term of flow resistance corresponds to a deceleration in flow and the predictor $\mathbf{u}_{w/o}$ may be retained as the new velocity value;
   b. if their scalar product is negative, the term of flow resistance results in reversal of the flow, which is not physically sound because in reality the fluid would stop such a case; therefore the new velocity value is simply set to zero.

4.3 Model verification

Examples of model verification are presented here, namely a slump test, treated with both Bingham and frictional fluid rheological models, as well as a case of failure of a real tailing dam. More model verifications will be detailed in subsequent contributions, enabling to systematically validate all components of the model, including the purely viscous stresses, yield stress as well as their one- and two-dimensional implementations.

Slump test

The slump test consists in the sudden release of a cone of material which was previously confined. For a Bingham fluid, the one-dimensional profile of the material at the end of the test corresponds to an analytical solution of the system of equations (61)-(62), combined with the flow resistance formula (55). Indeed, when the flow stops, all velocity components are zero and only the following terms remain in equation (62), expressing the balance between the surface slope and the yield stress:

$$-\frac{\partial}{\partial x}\left(\rho g\frac{h^2}{2}\right)-\tau_0=0 \qquad \Rightarrow \qquad h=h_0\sqrt{1-\frac{2\tau_0}{\rho g h_0}\frac{x}{h_0}}\,. \tag{64}$$

This leads to a parabolic free surface profile when the material freezes (Fig. 10), the shape of which depends on the yield stress τ_0 and the initial height of the material h_0.
The model has been similarly verified for the frictional fluid rheological model. Numerical predications could be successfully compared with those from the model by Manganey-Castelnau (2005).

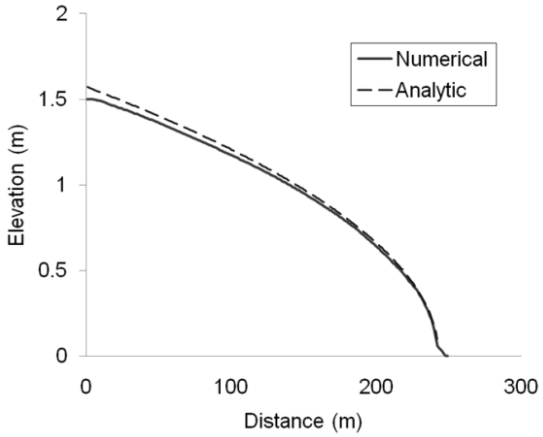

Fig. 10. Numerical predictions (Bingham model) vs. analytical solution for the slump test.

Gypsum tailing dam

Jeyapalan et al. (1983) described the flow of liquefied mine residues following the failure of the "Gypsum Dam" in Texas in 1966. The deposits were confined inside a rectangular reservoir with a depth of 11m at the time of the accident. Following seepage at the toe, a 140m breach opened up in the dike. The flow stretched to over 300m in length, with velocities in the order of 2.5 to 5 m/s. The material was characterised by a mean diameter of 70 microns and a density of 2,450 kg/m^3.
Consistently with Pastor et al. (2002), the simulation has been conducted using the Bingham fluid rheological model, with a yield stress $\tau_0 = 10^3$ Pa and a viscosity $\mu = 50$ Pa s. The density of the mixture was estimated at 1,400 kg/m^3.
Fig. 11 shows the agreement between the reference results by Pastor et al. (2002) and the predictions of the model developed here. In particular, a hydraulic jump appears around $t = 60$ s, following the stoppage of material situated along the breach axis, while the flow continues laterally until around $t = 120$ s in the more upstream part the wave.

5. Conclusion

Numerous issues remain challenging in current modelling capacities of flow, sediment transport and morphodynamics. In this chapter we have addressed two of them, namely handling mixed alluvial and non-alluvial beds and modelling hyperconcentrated flows.
Those two topics have been analyzed within an original modelling framework developed by the authors. It relies on a two-phase flow model set up to describe the flow of water-sediment mixtures. Increased inertia of the mixture as a result of the sediment concentration is accounted for in the momentum equations, which is hardly ever the case in currently

available morphodynamic models. To this end, the local continuity and momentum equations for the mixture have been depth-averaged without assuming straightaway particular concentration and velocity profiles, resulting in a generalized formulation of depth-averaged equations for water-sediment mixtures.

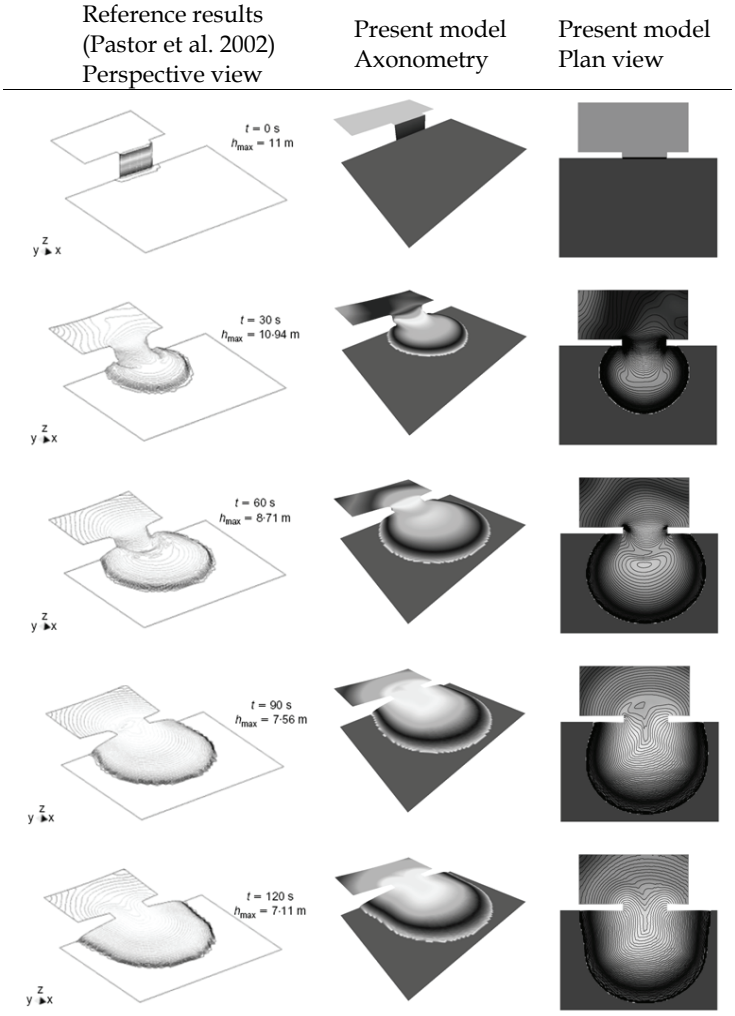

Fig. 11. Reference results in perspective (left), axonometric view and plan view of predictions of the model developed here for the "Gypsum dam" collapse.

In addition, an existing finite volume model for shallow flows has been accommodated to solve the generalized two-phase model for water-sediment mixtures. The stability of the extended scheme was demonstrated by Dewals (2006) and the resulting model succeeds in handling the wide range of time scales involved in practical sediment transport problems (Dewals et al. 2008a). Indeed, as a result of the flexibility offered in the levels of coupling

between flow and sediment transport models, stable and accurate numerical solutions are obtained in a realistic CPU time for predictions of erosion and sedimentation patterns in the short, medium or long term, considering both bed-load and suspended load.
The set of governing equations has subsequently been particularized for two specific configurations, namely bed-load transport on partly non-alluvial beds and rapid runout of hyperconcentrated flows such as flowslides, mudflows or debris flows.
A unified algorithm with correction on the outward fluxes of the continuity equations in fluid mixture and sediment layer has been implemented in our two-phase depth-averaged flow model in order to deal with drying cells and sediment routing over partly non-alluvial beds. Our original contribution lies here in the unified mathematical treatment of these two issues. The new procedure has been successfully verified on three test cases, in which the flow and sediment mass conservation error has been shown to remain of the order of the floating-point accuracy.
Finally, our two-phase depth-averaged flow model has been adapted to account for the particular rheology of hyperconcentrated flows, including visco-plasticity and frictional behaviour influenced by pore pressure. A depth-averaged formulation of these rheological models has been derived. Based on mass and momentum conservation for the mixture of sediment and interstitial fluid, the resulting finite volume model has been shown to handle successfully flow initiation, propagation (including on dry areas) and stoppage consistently with the yield stress behaviour observed in nature and experiments. An original numerical treatment of the yield stress has been presented and applies for multidimensional problems, both for the Bingham fluid and the frictional fluid models. This newly elaborated model has been verified by comparison with a number of experimental, numerical and field data; and is readily available for practical applications such as flowslide hazard mapping and emergency planning. The feasibility and opportunity to develop a rheological model further integrating the “Bingham fluid” and “frictional fluid” approaches will be explored in future research.

6. References

Audusse, E., Bouchut, F., Bristeau, Klein, R., and Perthame, B. (2004). "A Fast and Stable Well-Balanced Scheme with Hydrostatic Reconstruction for Shallow Water Flows." *SIAM J. Sci. Comput.*, 25(6), 2050-2065.

Begnudelli, L., and Sanders, B. F. (2007). "Conservative Wetting and Drying Methodology for Quadrilateral Grid Finite-Volume Models." *Journal of Hydraulic Engineering*, 133(3), 312-322.

Bombardelli, F., and Jha, S. (2009). "Hierarchical modeling of the dilute transport of suspended sediment in open channels." *Environmental Fluid Mechanics*, 9(2), 207-235.

Cao, Z., and Carling, P. A. (2002a). "Mathematical modelling of alluvial rivers: reality and myth. Part 1: General review." *Water & Maritime Engineering*, 154(3), 207-219.

Cao, Z., and Carling, P. A. (2002b). "Mathematical modelling of alluvial rivers: reality and myth. Part 2: Special issues." *Water & Maritime Engineering*, 154(4), 297-307.

Cao, Z., Day, R., and Egashira, S. (2002). "Coupled and Decoupled Numerical Modeling of Flow and Morphological Evolution in Alluvial Rivers." *Journal of Hydraulic Engineering*, 128(3), 306-321.

Cao, Z., Wei, L., and Xie, J. (1995). "Sediment-Laden Flow in Open Channels from Two-Phase Flow Viewpoint." *Journal of Hydraulic Engineering*, 121(10), 725-735.

Dewals, B., Archambeau, P., Erpicum, S., Mouzelard, T., and Pirotton, M. (2002a). "Coupled computations of highly erosive flows with WOLF software." *Proc. 5th Int. Conf. on Hydro-Science & -Engineering*, Warsaw, 10 p.

Dewals, B., Archambeau, P., Erpicum, S., Mouzelard, T., and Pirotton, M. (2002b). "Dam-break hazard mitigation with geomorphic flow computation, using WOLF 2D hydrodynamic software." Risk Analysis III, C. A. Brebbia, ed., WIT Press, 59-68.

Dewals, B., Archambeau, P., Erpicum, S., Mouzelard, T., and Pirotton, M. (2002c). "An integrated approach for modelling gradual dam failures and downstream wave propagation." *Proc. 1st IMPACT Project Workshop*, Wallingford.

Dewals, B. J. (2006). "Une approche unifiée pour la modélisation d'écoulements à surface libre, de leur effet érosif sur une structure et de leur interaction avec divers constituants," PhD Thesis, University of Liege, Liège.

Dewals, B. J., Erpicum, S., Archambeau, P., Detrembleur, S., Fraikin, C., and Pirotton, M. (2004). "Large scale 2D numerical modelling of reservoirs sedimentation and flushing operations." *Proc. 9th Int. Symposium on River Sedimentation*, Yichang, Chine.

Dewals, B. J., Erpicum, S., Archambeau, P., Detrembleur, S., and Pirotton, M. (2006). "Depth-integrated flow modelling taking into account bottom curvature." *J. Hydraul. Res.*, 44(6), 787-795.

Dewals, B. J., Erpicum, S., Archambeau, P., Detrembleur, S., and Pirotton, M. (2008a). "Hétérogénéité des échelles spatio-temporelles d'écoulements hydrosédimentaires et modélisation numérique." *Houille Blanche-Rev. Int.*(5), 109-114.

Dewals, B. J., Erpicum, S., Detrembleur, S., Archambeau, P., and Pirotton, M. (2010a). "Failure of dams arranged in series or in complex." *Natural Hazards*, Published online: 27 Aug. 2010. DOI: 10.1007/s11069-010-9600-z.

Dewals, B. J., Kantoush, S. A., Erpicum, S., Pirotton, M., and Schleiss, A. J. (2008b). "Experimental and numerical analysis of flow instabilities in rectangular shallow basins." *Environ. Fluid Mech.*, 8, 31-54.

Dewals, B. J., Rulot, F., Erpicum, S., Archambeau, P., and Pirotton, M. (2010b). "Long-term sediment management for sustainable hydropower." Comprehensive Renewable Energy. Volume 6 - Hydro Power, A. Sayigh, ed., Elsevier, Oxford.

Ernst, J., Dewals, B. J., Detrembleur, S., Archambeau, P., Erpicum, S., and Pirotton, M. (2010). "Micro-scale flood risk analysis based on detailed 2D hydraulic modelling and high resolution land use data." Nat. Hazards, 55 (2), 181-209.

Erpicum, S., Dewals, B. J., Archambeau, P., Detrembleur, S., and Pirotton, M. (2010a). "Detailed inundation modelling using high resolution DEMs." *Engineering Applications of Computational Fluid Mechanics*, 4(2), 196-208.

Erpicum, S., Dewals, B. J., Archambeau, P., and Pirotton, M. (2010b). "Dam-break flow computation based on an efficient flux-vector splitting." *Journal of Computational and Applied Mathematics*, 234(7), 2143-2151.

Erpicum, S., Meile, T., Dewals, B. J., Pirotton, M., and Schleiss, A. J. (2009). "2D numerical flow modeling in a macro-rough channel." *Int. J. Numer. Methods Fluids*, 61(11), 1227-1246.

Fraccarollo, L., and Capart, H. (2002). "Riemann wave description of erosional dam-break flows." *J. Fluid Mech.*, 461, 183-228.

Frey, P., and Church, M. (2009). "How River Beds Move." *Science*, 325(5947), 1509-1510.

Gourgue, O., Comblen, R., Lambrechts, J., Kärnä, T., Legat, V., and Deleersnijder, E. (2009). "A flux-limiting wetting-drying method for finite-element shallow-water models, with application to the Scheldt Estuary." *Advances in Water Resources*, 32(12), 1726-1739.

Greco, M., Iervolino, M., Vacca, A., and Leopardi, A. (2008). "A two-phase model for sediment transport and bed evolution in unsteady river flow." River flow 2008, Altinakar, Kirkgoz, Kokpinar, Aydin, and Cokgor, eds., Izmir, Turkey.

Greimann, B. P., and Holly, F. M. (2001). "Two-Phase Flow Analysis of Concentration Profiles." *Journal of Hydraulic Engineering*, 127(9), 753-762.

Greimann, B. P., Muste, M., and Holly, F. M. J. (1999). "Two-phase Formulation of Suspended Sediment Transport." *Journal of Hydraulic Research*, 37(4), 479-491.

Hervouet, J.-M. (2003). *Hydrodynamique des écoulements à surface libre - Modélisation numérique avec la méthode des éléments finis*, Presses de l'école nationale des Ponts et Chaussées, Paris.

Hervouet, J., Machet, C., and Villaret, C. (2003). "Calcul des évolutions sédimentaires : le traitement des fonds rigides." *Revue européenne des éléments finis*, 12(2-3), 221-234.

Hungr, O. (1995), *A model for the runout analysis of rapid flow slides, debris flows, and avalanches*, Canadian Geotechnical Journal, 32 (4), 610-623.

Hutchinson, J. N. (1986), *A sliding-consolidation model for flow slides*, Canadian Geotechnical Journal, 23 (2), 115-126.

Jeyapalan, J. K., Duncan, and Seed. (1983). "Investigation of flow failures of tailings dams." *Journal of Geotechnical Engineering*, 109(2), 172-189.

Kaitna, R., and Rickenmann, D. (2007). "A new experimental facility for laboratory debris flow investigation." *Journal of Hydraulic Research*, 45(6), 797-810.

Kerger, F., Archambeau, P., Erpicum, S., Dewals, B. J., and Pirotton, M. (2010a). "A fast universal solver for 1D continuous and discontinuous steady flows in rivers and pipes." *Int. J. Numer. Methods Fluids*, Published online: 29 Dec 2009. DOI: 10.1002/fld.2243.

Kerger, F., Erpicum, S., Dewals, B., Archambeau, P., and Pirotton, M. (2010b). "1D Unified Mathematical Model for Environmental Flow Applicated to Aerated Mixed Flows." *Advances in Engineering Software*, In press.

Kerger, F., Dewals, B., Archambeau, P., Erpicum, S. and Pirotton, M. (2011), *A Multiphase Model for the Transport of Dispersed Phases in Environmental Flows: Theoretical Contribution*, European Journal of Mechanical and Environmental Engineering, In press.

Khuat Duy, B., Archambeau, P., Dewals, B. J., Erpicum, S., and Pirotton, M. (2010). "River modelling and flood mitigation in a Belgian catchment." *Proc. Inst. Civil. Eng.-Water Manag.*, 163(8), 417-423.

Kleinhans, M. G., Jagers, H. R. A., Mosselman, E., and Sloff, C. J. (2008). "Bifurcation dynamics and avulsion duration in meandering rivers by one-dimensional and three-dimensional models." *Water Resources Research*, 44, 31 PP.

Laigle, D., and Coussot, P. (1997). "Numerical modeling of mudflows." *Journal of Hydraulic Engineering*, 123(7), 617-623.

Leal, J. G. A. B., Ferreira, R. M. L., and Cardoso, A. H. (2003). "Dam-break wave propagation over a cohesionless erodible bed." Proc. 30rd IAHR Congress, J. Ganoulis and P. Prinos, eds., IAHR, Thessaloniki, Grèce, 261-268.

Mangeney-Castelnau, A., Bouchut, F., Vilotte, J. P., Lajeunesse, E., Aubertin, A., and Pirulli, M. (2005). "On the use of Saint Venant equations to simulate the spreading of a granular mass." *J. Geophys. Res*, 110, B09103.

Morris, M., and Galland, J. (2000). "CADAM, Dambreak Modelling Guidelines & Best Practice." European Commission.

Nikora, V., McEwan, I., McLean, S., Coleman, S., Pokrajac, D., and Walters, R. (2007). "Double-Averaging Concept for Rough-Bed Open-Channel and Overland Flows: Theoretical Background." *Journal of Hydraulic Engineering*, 133(8), 873-883.

Pastor, M., Quecedo, M., Gonzalez, E., Herreros, M. I., Merodo, J. A. F., Merodo, J. A. F., and Mira, P. (2004). "Simple approximation to bottom friction for Bingham fluid depth integrated models." *Journal of Hydraulic Engineering*, 130(2), 149-155.

Pastor, M., Quecedo, M., Merodo, J. A. F., Herrores, M. I., Gonzalez, E., and Mira, P. (2002). "Modelling tailings dams and mine waste dumps failures." *Geotechnique*, 52(8), 579-591.

Quecedo, M., Pastor, M., Herreros, M. I., and Merodo, J. (2004). "Numerical modelling of the propagation of fast landslides using the finite element method." *Int. J. Numer. Methods Engng*, 59, 755-794.

Roger, S., Dewals, B. J., Erpicum, S., Schwanenberg, D., Schüttrumpf, H., Köngeter, J., and Pirotton, M. (2009). "Experimental und numerical investigations of dike-break induced flows." *J. Hydraul. Res.*, 47(3), 349-359.

Spasojevic, M., and Holly, F. M. (2008). "Two- and thre-dimensional numerical simulation of mobile-bed hydrodynamics and sedimentation." Sedimentation engineering : processes, measurements, modeling, and practice, H. G. Marcelo, ed., American Society of Civil Engineers, 683-761.

Struiksma, N. (1999). "Mathematical modelling of bedload transport over non-erodible layers." *Proceedings of IAHR Symposium on River, Coastal and Estuarine Morphodynamics*, Genova, 6-10.

van Rijn, L. C. (2007). "Unified View of Sediment Transport by Currents and Waves. I: Initiation of Motion, Bed Roughness, and Bed-Load Transport." *Journal of Hydraulic Engineering*, 133(6), 649-667.

van Rijn, L. C., Walstra, R., and Ormondt, M. v. (2007). "Unified View of Sediment Transport by Currents and Waves. IV: Application of Morphodynamic Model." *Journal of Hydraulic Engineering*, 133(7), 776-793.

Walters, R., and Plew, D. (2008). "Numerical modeling of environmental flows using DAM: Some preliminary results." *Acta Geophysica*, 56, 918-934.

White, R. (2001). *Evacuation of sediments from reservoirs*, Thomas Telford.

Wu, W. M., and Wang, S. S. (2000). "Mathematical models for liquid-solid two-phase flow." *Int J Sediment Res*, 15(3), 288-298.